HHS Public Access

Author manuscript

Cell Rep. Author manuscript; available in PMC 2024 August 09.

Published in final edited form as:

Cell Rep. 2024 June 25; 43(6): 114334. doi:10.1016/j.celrep.2024.114334.

Tentonin 3 is a pore-forming subunit of a slow inactivation mechanosensitive channel

Sungmin Pak[1,2,10], **Hyunil Ryu**[1,10], **Sujin Lim**[1,9], **Thien-Luan Nguyen**[1,2], **Sungwook Yang**[3], **Sumin Kang**[4], **Yeon Gyu Yu**[4], **Junhyuk Woo**[1], **Chanjin Kim**[1], **Cristina Fenollar-Ferrer**[5,6], **John N. Wood**[7], **Mi-Ock Lee**[2], **Gyu-Sang Hong**[1,8,9,*], **Kyungreem Han**[1,8,*], **Tae Song Kim**[1,*], **Uhtaek Oh**[1,9,11,*]

[1]Brain Science Institute, Korea Institute of Science and Technology (KIST), Seoul 02792, Korea

[2]College of Pharmacy, Seoul National University, Seoul 08826, Korea

[3]Artificial Intelligence and Robotics Institute, KIST, Seoul 02792, Korea

[4]Department of Chemistry, Kookmin University, Seoul 02707, Korea

[5]Stiles-Nicholson Brain Institute at Florida Atlantic University, Jupiter, FL 33458, USA

[6]Laboratory of Molecular Genetics, NIDCD, NIH, Bethesda, MD 20892, USA

[7]Molecular Nociception Group, Wolfson Institute for Biomedical Research, University College London, London WC1E 6BT, UK

[8]Division of Bio-Medical Science & Technology, KIST School, University of Science and Technology, Seoul 02792, Korea

[9]Department of Molecular Medicine and Biopharmaceutical Sciences, Graduate School of Convergence Science and Technology, Seoul National University, Seoul 08826, Korea

[10]These authors contributed equally

[11]Lead contact

SUMMARY

Mechanically activating (MA) channels transduce numerous physiological functions. Tentonin 3/TMEM150C (TTN3) confers MA currents with slow inactivation kinetics in somato- and barosensory neurons. However, questions were raised about its role as a Piezo1 regulator and

*Correspondence: gshong@kist.re.kr (G.-S.H.), khan@kist.re.kr (K.H.), tskim@kist.re.kr (T.S.K.), utoh@kist.re.kr (U.O.).

AUTHOR CONTRIBUTIONS

S.P., S.L., T.-L.N., and G.-S.H. performed TTN3 ortholog cloning, mutations of TTN3, and patch-clamp experiments; S.K. and Y.G.Y. performed TTN3 protein purification; H.R. performed electrophysiology in the lipid bilayer; T.S.K. designed and performed data analysis of electrophysiology; S.Y. gave technical assistance for mechanical stimulation; K.H. designed the computational analysis and performed MD simulations; J.W., C.K., C.F.-F., and K.H. performed TTN3 modeling; J.N.W. and M.-O.L. supervised pharmacology experiments; and U.O. designed and supervised experiments and wrote the manuscript.

SUPPLEMENTAL INFORMATION

Supplemental information can be found online at https://doi.org/10.1016/j.celrep.2024.114334.

DECLARATION OF INTERESTS

The authors declare no competing interests.

its potential as a channel pore. Here, we demonstrate that purified TTN3 proteins incorporated into the lipid bilayer displayed spontaneous and pressure-sensitive channel currents. These MA currents were conserved across vertebrates and differ from Piezo1 in activation threshold and pharmacological response. Deep neural network structure prediction programs coupled with mutagenetic analysis predicted a rectangular-shaped, tetrameric structure with six transmembrane helices and a pore at the inter-subunit center. The putative pore aligned with two helices of each subunit and had constriction sites whose mutations changed the MA currents. These findings suggest that TTN3 is a pore-forming subunit of a distinct slow inactivation MA channel, potentially possessing a tetrameric structure.

Graphical abstract

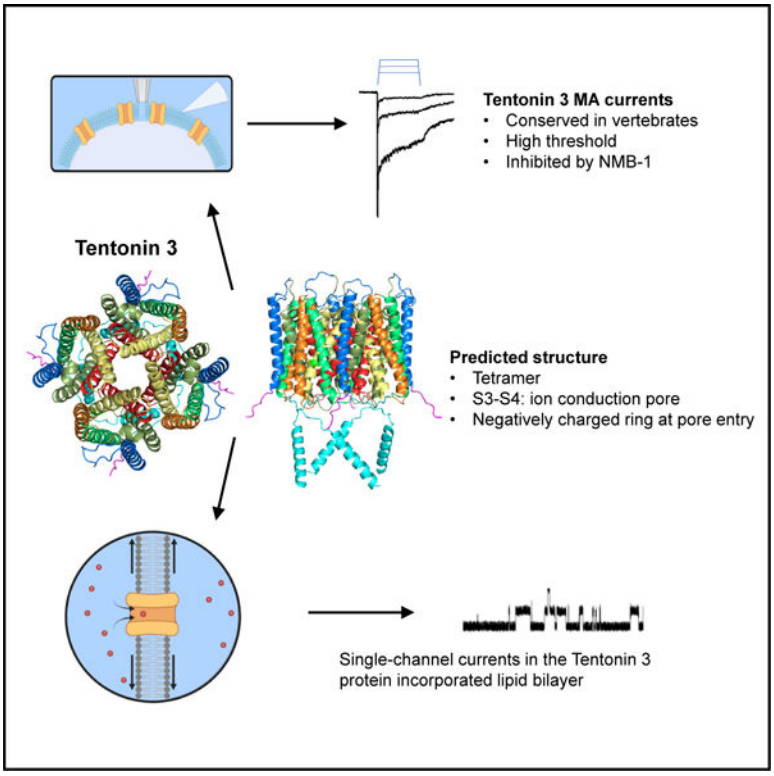

In brief

Pak et al. reveal Tentonin 3/TMEM150C (TTN3) as a slowly adapting mechanosensitive channel conserved within the vertebrate phyla eliciting stretch-sensitive currents. TTN3 activation requires high-threshold stimulation and is inhibited by NMB-1. Further on, structure-predicting algorithmic programs reveal TTN3 as a rectangular-shaped tetrameric structure forming a pore at the center.

INTRODUCTION

Mechanotransduction is a fundamental biological mechanism that is necessary for physiological functions such as somatosensation, motor coordination, baroreceptor reflex, hearing, and pain reception.[1,2] Perceiving the mechanical stimuli for these functions begins

with the mechanically activating (MA) channels in the sensory end organs that convert mechanical stimuli into electrical signals.[3] In the dorsal root ganglion (DRG) neurons that detect touch, pressure, vibration, and mechanical pain, there are three types of native MA currents,[2–4] namely rapidly adapting (RA), slowly adapting (SA), and intermediately adapting (IA) currents, depending on their inactivation times. These distinct MA currents are also observed in the baroreceptor neurons of the nodose ganglia.[5]

Many candidate genes have been identified in various animal species for their mechanosensitivity. Piezo channels are activated by mechanical indentation with RA and possibly IA kinetics.[6,7] The Piezo channels are differentially expressed in numerous cell types and mediate diverse physiological and cellular functions.[8] Therefore, their dysfunction in humans causes numerous hereditary diseases.[9] Cryoelectron micrograph analysis has revealed the unique molecular structure of Piezo1, which has a propeller blade-like shape and a concave body that easily senses change in membrane tension.[8,10,11] TMEM120A (TACAN) was proposed as an ion channel candidate for SA-type MA currents in DRG neurons sensing nociceptive mechanical pain.[12] However, following literatures reveal TACAN as a negative regulator for Piezo2 channels and also show TACAN to be structurally similar to a lipid-modifying enzyme.[13–15]

Tentonin 3/TMEM150c (TTN3) was identified to be a gene responsible for the SA-type MA currents in the DRG neurons.[4] The heterologous expression of TTN3 gave rise to robust currents in response to mechanical step stimuli, with two inactivation phases: a rapid and then a slow inactivation.[4] Genetic deletion of the *Ttn3* gene in DRG and nodose ganglion neurons ablates the SA-type MA currents.[4,5] Moreover, TTN3 is expressed in muscle spindles, baroreceptors, and pancreatic β-cells, and its ablation results in a loss of muscle coordination, blood pressure control, and insulin release, respectively.[4,5,16] Despite these findings, recently published literature shows conflicting data portraying TTN3 as not contributing to the production of SA-type MA currents and proprioceptive phenotypes.[17–19] Because TTN3 MA currents were lost in *Piezo1*-knockout HEK (human embryonic kidney) 293T cells (HEK-P1KO), its mechanosensitivity was questioned and considered as a regulator of Piezo1.[17,19,20] However, the pre-treatment of jasplakinolide, a cytoskeleton enhancer, to HEK-P1KO cells exhibits robust TTN3 MA currents.[5] Thus, TTN3 appears to act as a channel independently from Piezo1. However, whether TTN3 is a *bona fide* MA channel with a pore-forming subunit is not yet determined. Therefore, the present study aimed to determine whether TTN3 is a pore-forming subunit of an MA channel. In addition, we utilized deep learning methods to achieve prediction accuracies greater than those of force-field-based approaches[21–23] to gain structural insight into TTN3 action.

RESULTS

Mechanosensitivity of TTN3 is conserved throughout the vertebrate phyla

Since TTN3 is expressed only in the vertebrate phyla,[4] its seven representative orthologs (Figure S1) were tested for their mechanosensitive properties. Step mechanical indentations (6.4–8.5 μm, 600 ms) with a glass microprobe elicited MA currents in HEK293T cells transfected with mouse (*Mus musculus*), zebrafish (*Danio rerio*), chick (*Gallus gallus*), human (*Homo sapiens*), cat (*Felis catus*), turtle (*Chrysemys picta bellii*), and frog (*Xenopus*

tropicalis) *Ttn3* (Figures 1A and S1). Among the orthologs, HEK293T cells transfected with zebrafish *Ttn3* (drTTN3) displayed the greatest MA current amplitude, whereas cells expressing turtle and frog *Ttn3* displayed the least response to the mechanical stimuli (Figure 1B). The five (mouse, human, zebrafish, cat, and chick) TTN3 orthologs demonstrated typical MA currents in response to mechanical step stimuli: a rapid activation followed by a rapid and slow inactivation.

The TTN3 orthologs showed displacement-response relationships. Among the orthologs, drTTN3 was most sensitive to mechanical stimuli, as the half-maximal displacement was significantly smaller than that of mouse TTN3 (mTTN3) (4.9 ± 0.6 vs. 6.5 ± 0.4 μm, $p < 0.05$, Student's *t* test) (Figure 1C). In addition, these TTN3 orthologs showed different sensitivity to gadolinium (Gd^{3+}), which is a non-selective blocker of MA channels. Mechanical-step-activated currents of mTTN3 were almost completely inhibited by 100 μM Gd^{3+} (Figures 1D and 1E).[4] However, drTTN3 showed only ~60% inhibition by 100 μM Gd^{3+} (Figures 1D and 1E). Thus, these results suggest that the mechanosensitivity of TTN3 was well conserved throughout the vertebrate phyla but with different mechanical and pharmacological sensitivities.

TTN3 in the lipid bilayer elicits spontaneous and stretch-activated channel currents

To determine if TTN3 retains a pore-forming subunit, we purified human TTN3 (hTTN3) and drTTN3 and incorporated the proteins into the lipid bilayer to determine their spontaneous and stretch-activated single-channel currents. We isolated hTTN3 and drTTN3 proteins from *Escherichia coli* and stabilized them with an amphiphilic polymer, alkyl polyglycoside, for better dispersion in the aqueous media (Figures S2A and S2B).[24] Proteoliposomes containing hTTN3 or drTTN3 were fused and reconstituted into a model 1,2-diphytanoyl-*sn*-glycero-3-phosphocholine (DPhPC) membrane spanning an 80–100 μm aperture in a polytetrafluoroethylene film between the *cis* and *trans* chambers (Figure S2C). We carefully observed the annulus of spanned membranes to check for a possible stretch activation due to the increase in the contact angle of the annulus.[25] For the positive control, proteoliposomes containing purified bacterial MscL proteins were incorporated into the DPhPC model membrane, which exhibited typical large and Gd^{3+} reversible single-channel currents (Figure S2D).[26] Similarly, spontaneous channel openings were observed in the membranes that were fused with the proteoliposomes containing hTTN3 or drTTN3 (Figures 2A and 2B). The mean amplitudes of the unitary single-channel currents of hTTN3 and drTTN3 at 100 mV were 4.21 ± 0.48 or 5.98 ± 0.92 pA, respectively (Figure 2C). Therefore, single-channel conductances for hTTN3 and drTTN3 were 42.1 ± 4.8 and 59.8 ± 9.2 pS, respectively. The mean amplitude of the single-channel currents of drTTN3 was significantly greater than that of hTTN3 (Figure 2C). The current and voltage relationships between the single-channel currents of both hTTN3 and drTTN3 were linear in a symmetric 150 mM KCl solution (Figure 2D). Consistent with the results of the whole-cell currents in HEK293T cells, drTTN3 was more active than hTTN3, as the open probability of drTTN3 was significantly ($p < 0.001$, Student's t test) greater than that of hTTN3 at 30 min after reconstitution (Figure 2E). Spontaneous channel currents of hTTN3 were completely blocked by Gd^{3+}, whereas those of drTTN3 were partially blocked (Figure 2F). The activity of these single-channel currents increased over time, and they eventually became

macroscopic currents (Figure 2G). Macroscopic currents of hTTN3 were also blocked by 20 μM of Gd^{3+}, whereas those of drTTN3 were partially blocked (Figures 2F–2H), thereby confirming the different Gd^{3+} sensitivities of hTTN3 and drTTN3 when expressed in HEK293T cells (Figure 1E).

Both hTTN3 and drTTN3 were sensitive to the stretches applied to the lipid bilayer. When 20 μL of the solution (equivalent to 0.42 mmH_2O) was added to a *cis* or *trans* chamber, an abrupt increase in reversible MA channel currents was observed in both hTTN3- and drTTN3-reconstituted membranes (Figures 2I and 2J). These MA currents were not observed in the blank lipid bilayer (Figure 2I). These results suggest that both hTTN3 and drTTN3 are pore-forming subunits that are sensitive to membrane stretch.

TTN3 mechanosensitivity is separate from Piezo1

To determine whether TTN3 and Piezo1 have a different sensitivity to mechanical stimuli, we measured the MA currents of both mTTN3 and mPiezo1 in response to different speeds (80–2,560 μm/s) of a mechanical step stimulus (8 μm). As shown in Figures 3A and 3B, step stimuli with a speed less than 160 μm/s rarely activated mTTN3, whereas a speed over 80 μm/s readily activated mPiezo1 when overexpressed in HEK293T cells (Figure 3A). The half-maximal speed of mPiezo1 was significantly lower than that of mTTN3 (Figure 3B). In addition, the threshold (10% maximal response) of mPiezo1 was also significantly lower than that of mTTN3. Thus, the sensitivity to mechanical stimuli of TTN3 was lower than that of Piezo1.

A mutant of a ρ-conotoxin (ρ-TIA), also known as noxious mechanosensation blocker 1 (NMB-1), is known to inhibit SA, but not RA, MA currents in DRG neurons.[27] Because TTN3 confers the SA-MA currents observed in DRG neurons,[4] NMB-1 would inhibit the TTN3 MA currents. Indeed, the application of 10 μM NMB-1 strongly inhibited the MA currents in TTN3-expressing cells (Figures 3C and 3D). In contrast, 10 μM NMB-1 failed to inhibit the Piezo1 MA currents (Figures 3C and 3D). In addition, Yoda1 is a selective agonist of Piezo1 known to slow the inactivation of Piezo1.[28] If the TTN3 mechanosensitivity was dependent on Piezo1, then Yoda1 would modulate the kinetics of TTN3. Consistent with previous reports,[28] the application of 10 μM Yoda1 to cells expressing Piezo1 increased the inactivation time without affecting the amplitude of the MA currents (Figures 3E and 3F). However, the application of Yoda1 to TTN3/HEK293T cells did not affect the TTN3 inactivation kinetics (Figures 3G and 3H). These differences in pharmacological profiles further indicate that TTN3 activation is separate from Piezo1 activity.

mTTN3 tetrameric structures predicted by deep-learning-based algorithms

Because state-of-the-art deep learning methods able to predict the native protein structures from their sequences with high confidence have been developed,[21,23,29] we sought to predict the TTN3 structure using these algorithms. First, we determined the subunit composition of the hTTN3 protein. We purified the protein, cross-linked it with bis(β-[4-azidosalicylamido]-ethyl)disulfide, and isolated it on SDS-PAGE (Figures S3A and S3C). The western blot analysis of the cross-linked hTTN3 suggested a tetrameric subunit

composition (Figure S3C). Furthermore, the tetrameric protein band was also observed in a non-denaturing gel (Figure S3D).

The native structure of the mTTN3 monomer was modeled using AlphaFold2.[21,23,29] The resulting structural model manifested six transmembrane α-helices (S1–S6) that have the highest accuracy scores calculated using the predicted local-distance difference test in AlphaFold2[21] (Figures 4A and S4A). This scoring function uses a per-residue measurement that evaluates the local distance differences between a computational model and the experimentally determined reference structure.[30] The extracellular loop between S1 and S2 and the C terminus also contained short α-helices (Figure 4A).

Upon confirming a tetrameric composition of the TTN3 proteins, the optimal tetrameric conformation of the monomers was generated via the high ambiguity-driven docking program.[31,32] The optimal orientation/conformation of the four monomers was determined by evaluating the tetramer's molecular mechanical potential energy as a sum of individual energy terms such as van der Waals, electrostatic, desolvation, and restraint violation energies in the presence of an explicit water model.[33] The obtained tetrameric structures were grouped into four representative configuration models based on the two most relevant energy terms—van der Waals and electrostatic energies (Figures 4B and 4C). All four model configurations demonstrated a pore-like cavity region in the inter-subunit center. However, the location and orientation of the transmembrane helices (S1–S6) relative to the center axis of the tetramer were different (Figure 4B). Each model had a most constricting residue in the putative central pore that could determine ion conduction. Glu127, Glu33, and Cys66 of configuration models 1–3, respectively, were positioned at the top of their pores, whereas the Trp98 residue of model 4 was positioned at the bottom of the pore (Figure 4B). We then substituted each of these residues with Ala and evaluated the changes in mechanosensitivity. The E127A mutant, located at the pore of configuration model 1, resulted in a complete reduction in the amplitudes of TTN3 MA currents (Figures 4D and 4E). Thus, configuration model 1 was selected as the most probable model representing the native tetrameric structure of mTTN3.

Predicted molecular structure of TTN3

The selected tetrameric structure revealed a square-shaped monomeric arrangement with a putative pore at the center of the complex (Figures 5A and S4B). Transmembrane helices S3 and S4 formed the inner columns, whereas S1, S2, S5, and S6 formed the outer columns facing the membrane lipids (Figures 5A–5C; Video S1). Three negatively charged residues, DEE125–127, were located near the pore entrance, constituting the negatively charged ring at the pore opening (Figure 5C). This feature is observed in many types of cation channels, including the acetylcholine receptor, L-type Ca^{2+} channel, and many K^+ channels.[34–39]

The structural change in response to lipid bilayer deformation during mechanical force was examined using all-atom molecular dynamics (MD) simulations, where the selected tetrameric TTN3 structure was embedded in the 1,2-dioleoyl-*sn*-glycero-3-phosphocholine bilayer in a 150 mM KCl solution. The bilayer was moderately pulled laterally by applying a surface tension of 5 dyn/cm parallel to the bilayer plane, while the pressure normal to the bilayer plane was set at 1 atm. The total bilayer surface area increased by 8.50% (averaged

over three replicas), while the membrane thickness was reduced by 5.10% after 500 ns simulations (Figure S5). This lateral deformation gave rise to structural reformations of the TTN3 tetramer. While the overall structure was similar, the upper part of the outer helices S5, S6, and S1 were moved outward (Figure 5D). The upper part of S4 was also moved outward, possibly providing a larger opening of the pore (Figure 5D). The cross-sectional diameter at the constricting region was estimated using the program HOLE[40] to increase it by up to 6.06 Å from the initial value of 2.08 Å (Figure 5E), suggesting it as a potential site for ion conductance upon activation of the protein.

TTN3 constitutes a putative pore region

The central cavity of the structure is extended from the top to bottom, and the hollow vase-like space has a wall surrounded by the S3 and S4 domains (Figure 5B; Video S1). S3 and S4 cross each other, and the top end of S4 and the bottom end of S3 comprises the upper and lower openings of the pore, respectively (Figures 5B and 5C). There are four constricting sites, E127, V131, F139, and W98, along the ion conduction pathway (Figure 5E). In addition to the diminished MA current with the E127A mutation (Figure 4D), we further mutated the other three constricting residues to cysteine to test the inhibition of MA currents by a sulfhydryl-modifying agent, methanethiosulfonate (MTSET).[41,42] We applied a 6.4 μm step stimulus repeatedly before and after 1 mM MTSET treatment. In the wild-type mTTN3, there are 28 Cys residues (seven Cys residues in each subunit, at amino acids 6, 66, 107, 143, 176, 202, and 223) (Figure S6). However, none of these are located in the putative pore lining. Consistent with this, the MTSET treatment failed to change the MA currents of the wild-type mTTN3. In contrast, the application of MTSET reduced the MA currents of V131C, F139C, I101C, and W98C mutants (Figures 5G and 5H), whereas the MTSET treatment failed to change the MA currents of the T133C mutant, whose side chain protrudes toward the hydrophobic transmembrane α-helices (Figures 5F and 5H). These results suggest that the four (E127, V131, F139, and W98) residues are aligned along the putative ion-conducting pathway.

DISCUSSION

Three distinct types of MA currents according to their inactivation kinetics were observed in the somato- and barosensory neurons.[2–5] Specific genes were identified for the biophysically defined MA currents. Piezo1 and −2 confer RA- and possibly IA-type MA currents,[6,7] whereas TTN3 mediates the SA-type MA currents.[4] The unique TTN3 MA currents with slow inactivation kinetics were conserved throughout the vertebrate orthologs. TTN3 fulfills the four criteria required for an MA channel[8]: (1) genetic ablation of TTN3 markedly reduced the amplitudes and proportions of SA-MA currents in mechanosensory cells[4,5,16]; (2) heterologous expression of TTN3 in mammalian cells produces MA channel currents (Figure 1)[20,43]; (3) genetic ablation of TTN3 elicits functional phenotypes in baroreceptors, proprioceptors, and pancreatic β-cells[4,5,16]; (4) reconstitution of purified TTN3 protein into a lipid bilayer generated spontaneous and pressure-induced channel currents (Figure 2); and (5) NMB-1, known to inhibit SA currents in DRG neurons, inhibited TTN3 (Figures 3C and 3D).

Because TTN3 is not activated by mechanical stimuli in the absence of Piezo1, TTN3 is considered to be a regulator of Piezo1.[17,20] Since the genetic deletion of *Piezo1* or *Piezo2* impacts the cytoskeletal integrity,[44,45] *Piezo1* ablation in HEK293T cells may potentially influence the mechanosensitivity of TTN3 in *Piezo1*-ablated HEK293T cells. Indeed, mechanical stimuli failed to evoke MA currents in *Piezo1*-ablated HEK293T cells transfected with *Ttn3*.[5] However, after pre-treating the cells with an F-actin nucleation enhancer, jasplakinolide, the mechanical step stimuli were found to restore MA currents.[5] Conversely, disrupting the cytoskeleton with cytochalasin D led to the ablation of MA currents in *Ttn3*-transfected HEK293T cells.[5] These observations suggest that cytoskeletal integrity, compromised in *Piezo1*-deficient cells, might affect the mechanical force necessary to gate TTN3. As gating of TTN3 requires both forces, (1) cytoskeletal tethering and (2) membrane stretch, the absence of cytoskeletal proteins in artificial membranes brings about the question of how can TTN3 activity occur in proteoliposomes? If one of the two forces is higher than the activation threshold, then TTN3 will be opened by that corresponding force. Therefore, when the tension within the lipid bilayer reaches the activation threshold over time, TTN3 will be opened, regardless of the presence of cytoskeletons. Additionally, the thresholds for mechanical activation of TTN3 were significantly higher than those for Piezo1 (Figures 3A and 3B),[4] providing also a possible explanation for the observed loss of TTN3 MA currents in the absence of Piezo1.

Ojeda-Alonso and colleagues reported that the *Ttn3* ablation in mice fails to show phenotypes in electrophysiology as well as in *in vivo* experiments.[19] Specifically, they fail to find TTN3 mechanosensitivity in *Ttn3*-transfected *Piezo1*-deficient N2A ($N2A^{Piezo1-/-}$) cells despite observing Piezo1-dependent MA currents in these cells. As observed in *Piezo1*-deleted HEK293T cells, the genetic deletion of *Piezo1* in N2A cells may affect cytoskeleton integrity, which may lead to the absence of TTN3 MA currents in $N2A^{Piezo1-/-}$. In addition, Ojeda-Alonso and colleagues failed to find changes in nerve fiber activities of cutaneous mechanoreceptors in $Ttn3^{-/-}$ mice. Because TTN3 is rarely expressed in the skin, while it is greatly expressed in muscle spindles,[4] the contribution of TTN3 to mechanotransduction in mechanoreceptors would be minimal. Therefore, fiber activities of mechanoreceptors in the skin of wild-type and $Ttn3^{-/-}$ mice may not be different. Lastly, it is unclear why Ojeda-Alonso and colleagues found no phenotype with gait parameters of $Ttn3^{-/-}$ mice, whereas we found phenotypes in gait and other physiological functions between the two genotypes.[4,5,16] Sometimes, KO mice of the same channel gene elicit different behaviors.[46–49]

Despite the difference in structural, biophysical, and pharmacological profiles between TTN3 and Piezo1, many physiological functions of TTN3 overlap with those of Piezo channels, as both are expressed in muscle spindles and aortic baroreceptors, thereby mediating muscle coordination and blood pressure regulation, respectively.[4,5,16] The overlapping expressions and functions of the different molecules are not unusual, as they are seen in different transient receptor potential channels for temperature or pain sensing.[50,51] The redundancy of molecular sensors provides a backup system for the loss of key functions.

The predicted tetrameric model of TTN3 suggests a rectangular shape with a putative pore at the inter-subunit center. The pore in the center appears to be an ion conduction

lining because mutagenesis of the restricting residues markedly reduced the TTN3 currents. In the MD simulation, when tension was applied to the lipid bilayer, the size of the putative pore increased (Figures 5D and 5E), which may explain the activation of TTN3 through membrane tension. However, we cannot overlook the contribution of tethering to the subcellular structures, such as cytoskeletons. Although the structure modeling provided an insight into the overall structure of TTN3, the channel activation followed by inactivation through mechanical stimuli remains unknown. Structural information of the native form of TTN3 with cryoelectron microscopy analysis coupled with large-scale MD simulations would answer the detailed molecular mechanisms underlying its activation and inactivation.

Limitations of the study

One of the major limitations in further characterizing the molecular form of TTN3 is the lack of data provided by current protocols for determining its actual native structure. In this study, based on the molecular weight of TTN3, which approximately composes a tetrameric form, we managed to predict its molecular structure using deep learning algorithmic programs. Although the fidelity of computational programs capable of predicting a protein's native molecular structure has substantially increased, we cannot conclude that this model represents the actual structure of TTN3. Additionally, other machine learning algorithms for structure prediction such as AlphaFold-Multimer and MoLPC did not confirm the tetrameric structure of TTN3. Specialized protocols capable of visualizing the native structure of a protein, such as cryoelectron microscopy or X-ray crystallography, are required to consolidate the actual structural composition of TTN3.

As TTN3 confers mechanosensitive currents as a pore-forming subunit, the primary method for conducting mechanical stimulations in this study is through poking transfected cell lines with a blunt glass tip. Other mechanosensitive channels such as MscL, TREK, TRAAK, and Piezo respond to not only poking but also pressure, suction, or the pillar assay. It is challenging to understand why TTN3 does not evoke robust MA currents from certain mechanical stimulation apparatuses. TTN3's high mechanical threshold for activation might be one reason. However, further studies are required to elucidate this phenomenon.

STAR★METHODS

RESOURCE AVAILABILITY

Lead contact—Further information and requests for reagents may be directed to the lead contact, Uhtaek Oh (utoh@kist.re.kr).

Materials availability—This study did not generate new unique reagents.

Data and code availability

- The TTN3 monomer and tetramer models (in PDB format), initial coordinates, and the last 100-ns trajectories of all Molecular Dynamics simulations are available in a public repository, Zenodo Data: https://zenodo.org/record/8176280. Data are available from the corresponding author upon reasonable request.
- This paper does not report original code.

- Any additional information required to reanalyze the data reported in this paper is available from the lead contact upon request.

EXPERIMENTAL MODEL AND SUBJECT DETAILS

HEK293T (ATCC) cell line was maintained in Dulbecco's modified eagle medium (Gibco) supplemented with 10% fetal bovine serum (Gibco), and 1% penicillin-streptomycin (Gibco). The cell lines were maintained and cultured in a humidified incubator at 37°C with 5% CO_2.

Cells were seeded in 35 mm dishes and cultured until approximately 50% cell confluency was reached. At a 1:3 ratio of DNA to transfection reagent ratio, 1 μg of DNA was transfected with 3 mL of FuGENE HD transfection reagent (Promega) for 15 min. TTN3 ortholog constructs, murine TTN3 mutants, murine Piezo1, and GFP DNA constructs were subcloned into pIRES2-acGFP vectors and were utilised for transfection procedures. After 24 h, the transfected cells were collected and plated into 35 mm dishes containing glass coverslips, which were used for whole-cell patch-clamp recording the following day.

METHOD DETAILS

Gene preparation and mutagenesis—Tentonin 3/TMEM150C (TTN3) ortholog genes (mouse, zebrafish, frog, chick, turtle, cat, and human (Genscript)) were subcloned into pIRES2-acGFP vectors.[4,5] TTN3 target constructs were amplified with Dreamtaq Green Polymerase (Thermo Fisher Scientific) through PCR. DNA fragments separated in agarose gels were extracted and purified with FavorPrep Gel/PCR Purification Kit (Favorgen). The fragments underwent digestion with restriction enzymes (Thermo Fisher Scientific) and were ligated with T4 ligase (Thermo Fisher Scientific) using different molar insert-to-vector ratios; 1:1, 3:1, and 5:1. Transformation of the ligated products was performed with DH5α-chemically competent *E. Coli* (Enzynomics).

Mutants of mTTN3 were generated using either a Muta-Direct Site-directed Mutagenesis Kit (LiliF Diagnostics)) or EZchange Site-Directed Mutagenesis Kit (Enzynomics). The mutation products underwent transformation in DH5a-chemically competent *E. coli* cells and later cultured on Luria-Bertani (LB) agar plates. The TTN3 mutations in the constructs were confirmed through sequencing. The list of primers used for gene preparations can be seen in Table S1.

Whole cell current recording—Whole-cell currents of transfected HEK293T cells were recorded through the voltage-clamp technique. After forming a gigaseal with a glass pipette, the membrane patch under the glass pipette was ruptured with gentle suction to make a whole cell. Tip resistance of the glass pipettes was 2–3 MΩ. After forming a whole cell, capacitive transients were canceled. The holding potential was set at −60 mV. We recorded MA currents when the background currents were less than 100 pA. Whole cell currents were recorded with an Axopatch 200B amplifier (Molecular Devices). The amplifier output was filtered at 1 kHz and digitized with Digidata 1550B (Molecular Devices) at a sampling rate of 5 kHz and stored on a PC for later analysis. Whole cell currents were analyzed with Clampfit 10.0 software (Molecular Devices). The inactivation curves were fitted to

two exponentials. The intracellular (pipette) solution (mM) contained 130 CsCl, 2 $MgCl_2$, 4 Mg-ATP, 0.4 Na-GTP, 25 D-Mannitol and 10 HEPES. The extracellular (bath) solution (mM) contained 130 NaCl, 5 KCl, 1 $CaCl_2$, 2 $MgCl_2$, 10 D-Mannitol and 10 HEPES. The pH of both pipette and bath solutions were measured to 7.2 by adding CsOH and NaOH, respectively. All solution osmolarities were further adjusted to 295 mOsm with D-Mannitol. For the pharmacological experiments, $GdCl_3$, Yoda1, or NMB-1 (Smartox Biotechnology) or MTSET (Biotium) were added to the bath solution and incubated for 3 min after initial stimuli.

Mechanical stimulation—Whole cells of HEK293T cells transfected with various TTN3 orthologs or Piezo1 were physically stimulated with a glass pipette as previously described.[4,52] Briefly, after a glass pipette was pulled, the tip was fire-polished to produce a blunt tip 2–3 μm in diameter. The glass probe was fixed to the end of a Nano-controller NC4 micromanipulator (MM3A-LS, Kleindiek Nanotechnik). The movement of the glass probe was controlled with a joystick or via a computer program provided by Kleindiek. The nano-controller was a Piezo-driven small motor that had two modes of operation; fine and coarse movement mode. We calibrated the actual movements of the glass probe. In the coarse mode, the glass probe moved on average of 0.266 μm per step. Distances of the mechanical step stimuli were set at 24, 28 and 32 steps for 6.4, 7.4, and 8.5 μm displacement, respectively. We generally used the coarse 8 modes for mechanical stimulation, where the piezoelectric device vibrated at 2.7 kHz corresponding to the speed of 718 μm/s except for the speed-current relationship experiments. For the speed-current relationship experiments, the frequencies of the nano-controller motion were set at 0.3, 0.6, 1.2, 2.4, 4.8, and 9.6 kHz, which corresponded to the velocity being approximately 80, 160, 319, 638, 1277, and 2560 μm/s, respectively. The displacement of the probe was fixed at 8 μm for a 600 ms duration. Before physical indentation, the tip of the mechanical probe was placed on top of the cell surface at a 50° angle and withdrawn by 1 mm, which was regarded as an initial point for the mechanical step.

Expression and purification of hTTN3 in *E. coli*—The P9 sequence was attached to the N terminus of hTTN3 (or drTTN3) to facilitate the expression of hTTN3 in the membrane fraction of *E. coli*.[24] For the mass production of the P9-TTN3 fusion protein, BL21 (DE3) star-pRARE cells harboring the P9* expression vector, were grown in 5 mL LB containing 0.05 mg/mL carbenicillin and 0.05 mg/mL chloramphenicol for 16 h at 37°C. One milliliter of the pre-culture was inoculated into 50 mL of YTN (Yeast extract 1%, Bactotryptone 2%, NaCl 2%) medium containing 0.05 mg/mL carbenicillin and 0.05 mg/mL chloramphenicol and cultured at 37°C until the OD_{600nm} reached 1.0. One-third of the culture was inoculated into 150 mL of the YTN medium containing 0.05 mg/mL carbenicillin and 0.05 mg/mL chloramphenicol and cultured at 37°C until the OD_{600nm} reached between 1.0 and 2.0. The culture was then inoculated into a fermenter (Marado-PDA) containing 2 L culture medium (K_2HPO_4 0.3%, KH_2PO_4 0.5%, Yeast extract 2%, glucose 2%, $MgSO_4 \cdot 7H_2O$ 0.06%) containing 0.05 mg/mL carbenicillin and 0.05 mg/mL chloramphenicol. The cells were grown at 37°C, pH 6.7–6.8 and P_{O2} of 30%–40%. The expression of P9-TTN3 was induced by the addition of 1 mM IPTG for 3 h at 37°C when the OD_{600nm} of the culture was 46. The pH of the culture in the fermenter was

maintained at 6.8 by the addition of a small volume of the feeding medium (yeast extract 27.4%, $(NH_4)_2SO_4$ 0.15%, glucose 21.1%, $MgSO_4 \cdot 7H_2O$ 0.1%). The cells were harvested by centrifugation for 20 min at 3,000 × g and stored at −80°C until further use.

Approximately 30 g of *E. coli* cells (wet weight) were resuspended in buffer A (50 mM Tris-HCl, pH 8.5, 1 mM EDTA) containing 1 mM phenylmethylsulphonyl fluoride (Merck) and 100 μg protease inhibitor cocktail (genDEPOT), and lysed using a microfluidizer M-110P (Microfluidics). The lysate was centrifuged at 15,000 × g for 30 min, and the resulting supernatant was further centrifuged at 100,000 × g for 1 h. The membrane fraction in the pellet was solubilised in treatment with buffer A containing 0.5% sarkosyl for 2 h at 4°C. After removing the insoluble materials by centrifugation at 30,000 × g for 30 min, the recombinant hTTN3 in the solubilised membrane fraction was purified using a Ni-NTA agarose (Qiagen) column. The fractions containing hTTN3 were mixed with 4 mg APG for 4 h at 4°C. The hTTN3 complexed with APG was further purified by size exclusion chromatography using a Superdex 200 Increase 10/300 GL column (GE Healthcare). Each fraction during the Ni-NTA column purification process was visualized by SDS-PAGE and Western blot analysis.

Western blot—The purified P9-hTTN3 proteins were mixed with 5X SDS sample buffer, incubated at room temperature for 10 min. For crosslinking sample preparation, bis(β-[4-azidosalicylamido]-ethyl) disulphide (BASED), was dissolved in DMSO at a concentration of 10 mM. The purified hTTN3 protein (0.1 mg/mL) was mixed with 0, 5, 10, or 15 μM of BASED under UV exposure at room temperature for 15 min and mixed with 5X SDS sample buffer. In non-denaturing conditions, HEK293T cells transfected with control vector (pIRES-acGFP) and pIRES-mTTN3 were collected by lysis buffer made according to the NativePAGE sample prep kit (Invitrogen) instructions. The collected lysates were processed to 3 rounds of freeze-thaw cycles in liquid nitrogen and suspended until the cell debris were completely lysed. After 1 h of centrifugation in 18,000 × g in 4°C, the supernatant was collected and measured for protein quantification using Pierce BCA protein assay (Thermofisher Scientific). The non-denaturing samples were mixed with 2X T/G Native Sample Buffer (Koma Biotech) without boiling.

Protein samples (15 μg) were loaded in 4%–15% Lumi-gel precast gels (Luminano). Samples were subjected to electrophoresis at 120 V, 70 mA for 60 min in denaturing running buffer (25 mM Tris, 192 mM Glycine, 0.1% SDS) on room temperature or non-denaturing running buffer (25 mM Tris, 192 mM Glycine) on ice. After electrophoresis, the blots were transferred to methanol-activated polyvinylidene difluoride (PVDF) membrane via wet transfer method. The blots were transferred at 70 V, 400 mA for 90 min in transfer buffer (25 mM Tris, 192 mM Glycine, 0.1% SDS and 2% methanol) on ice.

The transferred membranes were proceeded to non-specific blocking under 5% BSA in TBST at room temperature for 1 h and later incubated with either anti-TTN3 antibody (1:500) (ABN2266, Merck), anti-His tag (1:5000) (AB1187, Abcam), or anti-P9 (1:5000) (manufactured, Ab frontier) at 4°C overnight. The PVDF membranes were washed with 3 rounds of TBST for 5 min per round and incubated with anti-mouse IgG secondary antibody (1:5000) (A9044, Sigma Aldrich) for purified hTTN3 protein samples or anti-rabbit IgG

secondary antibody (1:5000) (#7074, Cell signaling) for the non-denaturing samples for 1 h in room temperature. After washing with TBST for 3 rounds, the blots were detected with ECL Prime Western Blotting System (GE Healthcare). Detected protein bands were visualized with ImageQuant Las 4000 imaging system (GE Healthcare).

Preparation of proteoliposome—Each 40 mg/mL of 1-palmitoyl-2-oleoyl-*sn*-glycero-3-phosphocholine (POPC) and 1-palmitoyl-2-oleoyl-*sn*-glycero-3-phosphoethanolamine (POPE) stock solution was dissolved in chloroform at a 1:1 ratio. The mixture was dried on a glass vial surface spread out as wide as possible under gentle N_2 gas blowing for 30 min. The dried lipid film was rehydrated over 12 h in 140 mM KCl and 10 mM HEPES buffer to a final concentration of 10 mg/mL. The liposome solution was sonicated for 10 min with a 40% amplitude using a probe tip sonicator (Q125, Qsonica). Impurities in the liposomal solution were removed by centrifugation at 10,000 × g for 1 min. Clear milky liposome solution was mixed with the solution containing purified hTTN3, drTTN3 or MscL proteins at a 2:1 ratio and incubated for more than 12 h at 22°C. The final lipid-to-protein ratio was 1:20,000. To remove residual APG, the proteoliposome solution was filtered using 10 k molecular weight cut-off Amicon centrifugal filters (Merck Millipore) at 15,400 3 g for 15 min. All prepared proteoliposomes were used within 12 h.

Formation of the lipid bilayer incorporated with hTTN3, drTTN3 or MscL—The lipid bilayer membrane was formed with 3% DPhPC dissolved in n-decane (MP Biomedicals) using the painting method. An aperture of 80–100 μm was created using a spark generator (EM-09A, DAEDALON) on a 10 μm thick polytetrafluoroethylene film. The polytetrafluoroethylene film was clamped between two 300-μL chambers covered with transparent glass on one side. Both chambers were then filled with physiological buffer (140 mM KCl, 10 mM HEPES) and the Ag/AgCl electrodes were placed in both chambers separately. Then 0.2 μL of the DPhPC solution was painted on the aperture using a gel loading pipette (Corning). The formation of the bilayer was confirmed by microscope and capacitance measurement. After the formation of the lipid bilayer, 10–20 μL of the prepared proteoliposome was added to the *cis* chamber. Purified hTTN3, drTTN3 or MscL proteins in the proteoliposome were successfully reconstituted into the spanned bilayer lipid membrane by fusion. To apply pressure to the bilayer lipid membrane, we added 20 μL of buffer solution to the trans chamber to increase the pressure. Subsequently, we added an equal volume of buffer to the cis chamber to balance the pressure at zero cmH_2O between the two chambers. We then removed 20 mL of buffer from the trans chamber, creating a negative pressure environment.

Single-channel currents of the lipid bilayers were recorded using a patch-clamp amplifier (Axopatch 200B; molecular device). The acquired signals were processed with Digidata 1440A (molecular device). Signal recording conditions included a 10 kHz software filter, 5 kHz lowpass filter and 50 kHz sampling rate with the appropriate voltage bias in all experiments.

Protein structure prediction—The monomeric structure of mTTN3 (UniProt ID: Q8C8S3) was predicted using the AlphaFold2 program (v2.1.2).[21] The standard algorithm that was used consisted of two transformer-based modules for the sequence-residue and

residue-residue pairwise features. The sequence-residue graph was built using the multiple sequence alignments (MSA) embedding with UniProt Reference Clusters 90 (Uniref. 90), Big Fantastic Database, Uniclust30, and MGnify databases (updated on 27 Nov 2021). The residue-residue graph contains information regarding the relationship between the residues. The MSA-based representation updates the residue-residue pair information through an element-wise outer product and sum over the MSA sequence dimension in the Evoformer block. Five initial models were created using different random seeds—while two models were generated using template structures, the others were generated without templates.[21] The quality of the predicted monomer structures was evaluated using the pLDDT metric[21] applied to the Cα atoms' distance differences between the predicted and target structures[30] (Figure S4).

The monomer model (i.e., the one with the highest pLDDT value) was subsequently used as input into the multi-body interface implemented in the HADDOCK program (version 2.4)[31,32] to generate the tetrameric structure. The computations were performed using the standard protocol where the center of mass and non-crystallographic symmetry restraints were applied. The multi-body protocol consists of two main steps. In the first step, a set of 10,000 tetrameric models were generated via rigid-body docking followed by a refinement iteration of the 400 best-scored models introducing semi-flexible conditions. In the second step, only the 200 best-scored models obtained in the semi-flexible docking iteration were refined in the presence of an explicit water model. In this step the molecular mechanics potential energy as the sum of the individual energy terms such as van der Waals, electrostatic, desolvation, and restraints violation energies were used to evaluate the optimal orientation/conformation of the tetrameric structures. The obtained tetrameric structures were grouped into four models (Models 1–4) according to the conformational similarity and two most relevant energy terms; van der Waals and electrostatic energies (Figures 4B and 4C).

The Model 1 group was further assessed with the ProQM program.[54] ProQM analysis showed that the highest accuracy for the model was the residues located at the six transmembrane helices (averaged ProQM score/residue: 0.695 ± 0.10) whereas the lowest accuracy was shown for the residues located at the C terminus (0.282 ± 0.18). The score for the transmembrane α-helices in the tetrameric complex was significantly higher than those of the monomer (0.572 ± 0.10) indicating that the tetrameric configuration might be preferred over the monomeric.

MD simulations—The mTTN3 tetramer incorporated into the explicit bilayer model was simulated at the atomic level to obtain the molecular conformations of mTTN3 in the lipid membrane environment. The protonation states of the amino acid residues of the mTTN3 tetramer were titrated at pH = 7.4 using PROPKA 3.1,[53] and the hydrogen bond network of the tetrameric structure was optimised via PDB2PQR 2.1.[55] The protein was then embedded into the 1,2-dioleoyl-*sn*-glycero-3-phosphocholine (DOPC) bilayer using CHARMM-GUI.[56] Each leaflet of the bilayer contained 350 DOPC. The system was fully hydrated with 130 TIP3P water per lipid.[57] Neutralising cations (four K^+ ions) for the negative charge of the protein and additional KCl salt were added to achieve a 150 mM KCl bulk concentration. A molecular snapshot of the MD simulation system is shown in the Figure S5A. Each system

was simulated for three replicas (R1, R2, R3) with different random seeds for the initial velocities. Table S2 summarizes the MD simulation setup. Table S2 summarizes the MD simulation setup.

Simulations were conducted using the OpenMM (version 7.6.0)[58] program. The coordinates of all the atoms in the MD system were adjusted to minimize the energy and heated to 293.15 K over 125 ps followed by system equilibration for 1.75 ns. The production simulation was run using a Langevin thermostat at 298.15 K with a collision frequency of 1/ps. A Monte Carlo barostat[59] specifically designed for membrane simulations was used. The pressure, normal to the membrane plane, was 1 atm, corresponding to the normal laboratory conditions, and the surface tension applied parallel to the plane at the water-lipid head group interface was set to 5 dyn/cm. This surface tension corresponded to the negative lateral pressure that is capable of activating mechanosensitive ion channels, such as MscL, by laterally stretching the bilayer.[60,61] The van der Waals term used a standard 6–12 LJ form with a force-switching function between 8 and 12 Å. Particle mesh Ewald was used for long-range electrostatic measurements beyond 12 Å. The integration time step equals 2 fs. Coordinate sets were saved for every 5 ps. The CHARMM C36 lipid[62] and protein[63] force fields were used. Three replicas were simulated with different random seeds for the initial velocities to ensure the convergence of the simulations.

QUANTIFICATION AND STATISTICAL ANALYSIS

All data presented in the figures represent the mean ± standard error of the mean (SEM) or standard deviation (SD). All data presented in the figures represent the mean ± standard error of the mean. Student's *t*-test was used to compare two means. One-way analysis of variance (ANOVA) followed by Tukey test was used to compare multiple means. $p < 0.05$ was considered as significant.

Supplementary Material

Refer to Web version on PubMed Central for supplementary material.

ACKNOWLEDGMENTS

This research was supported by the National Research Foundation of Korea (NRF-2020R1A3A300192913 and RS-2023-00254795, U.O.; NRF-2020R1C1C101024513 and NRF-2022M3E5E801739512, G.-S.H.; Mid-Career Research Program 2020R1A2C1101174, Y.G.Y.; and 2020R1A2C210036313, T.S.K.). U.O. and K.H. were funded by internal grants of the Korea Institute of Science and Technology (2E32231 and 2Z06588, respectively). C.F.-F. was funded by the NIDCD Intramural Research Funds (DC000039 to Thomas B. Friedman) and the Program in Computational Brain Science and Health funded by the Palm Health Foundation.

REFERENCES

1. Ranade SS, Syeda R, and Patapoutian A (2015). Mechanically Activated Ion Channels. Neuron 87, 1162–1179. 10.1016/j.neuron.2015.08.032. [PubMed: 26402601]
2. Delmas P, Hao J, and Rodat-Despoix L (2011). Molecular mechanisms of mechanotransduction in mammalian sensory neurons. Nat. Rev. Neurosci 12, 139–153. 10.1038/nrn2993. [PubMed: 21304548]
3. Hao J, and Delmas P (2010). Multiple desensitization mechanisms of mechanotransducer channels shape firing of mechanosensory neurons. J. Neurosci 30, 13384–13395. 10.1523/jneurosci.2926-10.2010. [PubMed: 20926665]

4. Hong GS, Lee B, Wee J, Chun H, Kim H, Jung J, Cha JY, Riew TR, Kim GH, Kim IB, and Oh U (2016). Tentonin 3/TMEM150c Confers Distinct Mechanosensitive Currents in Dorsal-Root Ganglion Neurons with Proprioceptive Function. Neuron 91, 708–710. 10.1016/j.neuron.2016.07.019.
5. Lu HJ, Nguyen TL, Hong GS, Pak S, Kim H, Kim H, Kim DY, Kim SY, Shen Y, Ryu PD, et al. (2020). Tentonin 3/TMEM150C senses blood pressure changes in the aortic arch. J. Clin. Invest 130, 3671–3683. 10.1172/jci133798. [PubMed: 32484458]
6. Coste B, Mathur J, Schmidt M, Earley TJ, Ranade S, Petrus MJ, Dubin AE, and Patapoutian A (2010). Piezo1 and Piezo2 are essential components of distinct mechanically activated cation channels. Science 330, 55–60. 10.1126/science.1193270. [PubMed: 20813920]
7. Hill RZ, Loud MC, Dubin AE, Peet B, and Patapoutian A (2022). PIEZO1 transduces mechanical itch in mice. Nature 607, 104–110. 10.1038/s41586-022-04860-5. [PubMed: 35732741]
8. Kefauver JM, Ward AB, and Patapoutian A (2020). Discoveries in structure and physiology of mechanically activated ion channels. Nature 587, 567–576. 10.1038/s41586-020-2933-1. [PubMed: 33239794]
9. Delmas P, Parpaite T, and Coste B (2022). PIEZO channels and new-comers in the mammalian mechanosensitive ion channel family. Neuron 110, 2713–2727. 10.1016/j.neuron.2022.07.001. [PubMed: 35907398]
10. Zhao Q, Zhou H, Chi S, Wang Y, Wang J, Geng J, Wu K, Liu W, Zhang T, Dong MQ, et al. (2018). Structure and mechanogating mechanism of the Piezo1 channel. Nature 554, 487–492. 10.1038/nature25743. [PubMed: 29469092]
11. Saotome K, Murthy SE, Kefauver JM, Whitwam T, Patapoutian A, and Ward AB (2018). Structure of the mechanically activated ion channel Piezo1. Nature 554, 481–486. 10.1038/nature25453. [PubMed: 29261642]
12. Beaulieu-Laroche L, Christin M, Donoghue A, Agosti F, Yousefpour N, Petitjean H, Davidova A, Stanton C, Khan U, Dietz C, et al. (2020). TACAN Is an Ion Channel Involved in Sensing Mechanical Pain. Cell 180, 956–967.e17. 10.1016/j.cell.2020.01.033. [PubMed: 32084332]
13. Rong Y, Jiang J, Gao Y, Guo J, Song D, Liu W, Zhang M, Zhao Y, Xiao B, and Liu Z (2021). TMEM120A contains a specific coenzyme A-binding site and might not mediate poking- or stretch-induced channel activities in cells. Elife 10, e71474. 10.7554/eLife.71474. [PubMed: 34409941]
14. Xue J, Han Y, Baniasadi H, Zeng W, Pei J, Grishin NV, Wang J, Tu BP, and Jiang Y (2021). TMEM120A is a coenzyme A-binding membrane protein with structural similarities to ELOVL fatty acid elongase. Elife 10, e71220. 10.7554/eLife.71220. [PubMed: 34374645]
15. Del Rosario JS, Gabrielle M, Yudin Y, and Rohacs T (2022). TMEM120A/TACAN inhibits mechanically activated PIEZO2 channels. J. Gen. Physiol. 154, e202213164. 10.1085/jgp.202213164. [PubMed: 35819364]
16. Wee J, Pak S, Kim T, Hong GS, Lee JS, Nan J, Kim H, Lee MO, Park KS, and Oh U (2021). Tentonin 3/TMEM150C regulates glucose-stimulated insulin secretion in pancreatic β-cells. Cell Rep. 37, 110067. 10.1016/j.celrep.2021.110067. [PubMed: 34852221]
17. Anderson EO, Schneider ER, Matson JD, Gracheva EO, and Bagriantsev SN (2018). TMEM150C/Tentonin3 Is a Regulator of Mechano-gated Ion Channels. Cell Rep. 23, 701–708. 10.1016/j.celrep.2018.03.094. [PubMed: 29669276]
18. Parpaite T, Brosse L, Séjourné N, Laur A, Mechioukhi Y, Delmas P, and Coste B (2021). Patch-seq of mouse DRG neurons reveals candidate genes for specific mechanosensory functions. Cell Rep 37, 109914. 10.1016/j.celrep.2021.109914. [PubMed: 34731626]
19. Ojeda-Alonso J, Bégay V, Garcia-Contreras JA, Campos-Pérez AF, Purfürst B, and Lewin GR (2022). Lack of evidence for participation of TMEM150C in sensory mechanotransduction. J. Gen. Physiol 154. 10.1085/jgp.202213098.
20. Dubin AE, Murthy S, Lewis AH, Brosse L, Cahalan SM, Grandl J, Coste B, and Patapoutian A (2017). Endogenous Piezo1 Can Confound Mechanically Activated Channel Identification and Characterization. Neuron 94, 266–270.e3. 10.1016/j.neuron.2017.03.039. [PubMed: 28426961]

21. Jumper J, Evans R, Pritzel A, Green T, Figurnov M, Ronneberger O, Tunyasuvunakool K, Bates R, Žídek A, Potapenko A, et al. (2021). Highly accurate protein structure prediction with AlphaFold. Nature 596, 583–589. 10.1038/s41586-021-03819-2. [PubMed: 34265844]
22. Baek M, DiMaio F, Anishchenko I, Dauparas J, Ovchinnikov S, Lee GR, Wang J, Cong Q, Kinch LN, Schaeffer RD, et al. (2021). Accurate prediction of protein structures and interactions using a three-track neural network. Science 373, 871–876. 10.1126/science.abj8754. [PubMed: 34282049]
23. Tunyasuvunakool K, Adler J, Wu Z, Green T, Zielinski M, Žídek A, Bridgland A, Cowie A, Meyer C, Laydon A, et al. (2021). Highly accurate protein structure prediction for the human proteome. Nature 596, 590–596. 10.1038/s41586-021-03828-1. [PubMed: 34293799]
24. Han SG, Baek SI, Son TJ, Lee H, Kim NH, and Yu YG (2017). Preparation of functional human lysophosphatidic acid receptor 2 using a P9(*) expression system and an amphipathic polymer and investigation of its in vitro binding preference to G(a) proteins. Biochem. Biophys. Res. Commun 487, 103–108. 10.1016/j.bbrc.2017.04.025. [PubMed: 28392399]
25. Beerlink A, Thutupalli S, Mell M, Bartels M, Cloetens P, Herminghaus S, and Salditt T (2012). X-Ray propagation imaging of a lipid bilayer in solution. Soft Matter 8, 4595–4601. 10.1039/C2SM00032F.
26. Häse CC, Le Dain AC, and Martinac B (1995). Purification and functional reconstitution of the recombinant large mechanosensitive ion channel (MscL) of Escherichia coli. J. Biol. Chem 270, 18329–18334. 10.1074/jbc.270.31.18329. [PubMed: 7543101]
27. Drew LJ, Rugiero F, Cesare P, Gale JE, Abrahamsen B, Bowden S, Heinzmann S, Robinson M, Brust A, Colless B, et al. (2007). High-threshold mechanosensitive ion channels blocked by a novel conopeptide mediate pressure-evoked pain. PLoS One 2, e515. 10.1371/journal.pone.0000515. [PubMed: 17565368]
28. Syeda R, Xu J, Dubin AE, Coste B, Mathur J, Huynh T, Matzen J, Lao J, Tully DC, Engels IH, et al. (2015). Chemical activation of the mechanotransduction channel Piezo1. Elife 4, e07369. 10.7554/eLife.07369. [PubMed: 26001275]
29. Del Alamo D, Sala D, McHaourab HS, and Meiler J (2022). Sampling alternative conformational states of transporters and receptors with AlphaFold2. Elife 11, e75751. 10.7554/eLife.75751. [PubMed: 35238773]
30. Mariani V, Biasini M, Barbato A, and Schwede T (2013). lDDT: a local superposition-free score for comparing protein structures and models using distance difference tests. Bioinformatics 29, 2722–2728. 10.1093/bioinformatics/btt473. [PubMed: 23986568]
31. van Zundert GCP, Rodrigues JPGLM, Trellet M, Schmitz C, Kastritis PL, Karaca E, Melquiond ASJ, van Dijk M, de Vries SJ, and Bonvin AMJJ (2016). The HADDOCK2.2 Web Server: User-Friendly Integrative Modeling of Biomolecular Complexes. J. Mol. Biol 428, 720–725. 10.1016/j.jmb.2015.09.014. [PubMed: 26410586]
32. Karaca E, Melquiond ASJ, de Vries SJ, Kastritis PL, and Bonvin AMJJ (2010). Building macromolecular assemblies by information-driven docking: introducing the HADDOCK multibody docking server. Mol. Cell. Proteomics 9, 1784–1794. 10.1074/mcp.M000051-MCP201. [PubMed: 20305088]
33. de Vries SJ, van Dijk ADJ, Krzeminski M, van Dijk M, Thureau A, Hsu V, Wassenaar T, and Bonvin AMJJ (2007). HADDOCK versus HADDOCK: new features and performance of HADDOCK2.0 on the CAPRI targets. Proteins 69, 726–733. 10.1002/prot.21723. [PubMed: 17803234]
34. Imoto K, Busch C, Sakmann B, Mishina M, Konno T, Nakai J, Bujo H, Mori Y, Fukuda K, and Numa S (1988). Rings of negatively charged amino acids determine the acetylcholine receptor channel conductance. Nature 335, 645–648. 10.1038/335645a0. [PubMed: 2459620]
35. Konno T, Busch C, Von Kitzing E, Imoto K, Wang F, Nakai J, Mishina M, Numa S, and Sakmann B (1991). Rings of anionic amino acids as structural determinants of ion selectivity in the acetylcholine receptor channel. Proc. Biol. Sci 244, 69–79. 10.1098/rspb.1991.0053. [PubMed: 1679551]
36. Brelidze TI, Niu X, and Magleby KL (2003). A ring of eight conserved negatively charged amino acids doubles the conductance of BK channels and prevents inward rectification. Proc. Natl. Acad. Sci. USA 100, 9017–9022. 10.1073/pnas.1532257100. [PubMed: 12843404]

37. Bahinski A, Yatani A, Mikala G, Tang S, Yamamoto S, and Schwartz A (1997). Charged amino acids near the pore entrance influence ion-conduction of a human L-type cardiac calcium channel. Mol. Cell. Biochem 166, 125–134. 10.1023/a:1006847632410. [PubMed: 9046029]
38. D'Avanzo N, Cho HC, Tolokh I, Pekhletski R, Tolokh I, Gray C, Goldman S, and Backx PH (2005). Conduction through the inward rectifier potassium channel, Kir2.1, is increased by negatively charged extracellular residues. J. Gen. Physiol 125, 493–503. 10.1085/jgp.200409175. [PubMed: 15824191]
39. Doyle DA, Morais Cabral J, Pfuetzner RA, Kuo A, Gulbis JM, Cohen SL, Chait BT, and MacKinnon R (1998). The structure of the potassium channel: molecular basis of K+ conduction and selectivity. Science 280, 69–77. 10.1126/science.280.5360.69. [PubMed: 9525859]
40. Smart OS, Neduvelil JG, Wang X, Wallace BA, and Sansom MS (1996). HOLE: a program for the analysis of the pore dimensions of ion channel structural models. J. Mol. Graph 14, 354–376. 10.1016/s0263-7855(97)00009-x. [PubMed: 9195488]
41. Oelstrom K, and Chanda B (2016). Congruent pattern of accessibility identifies minimal pore gate in a non-symmetric voltage-gated sodium channel. Nat. Commun 7, 11608. 10.1038/ncomms11608. [PubMed: 27186888]
42. Zhao Q, Wu K, Geng J, Chi S, Wang Y, Zhi P, Zhang M, and Xiao B (2016). Ion Permeation and Mechanotransduction Mechanisms of Mechanosensitive Piezo Channels. Neuron 89, 1248–1263. 10.1016/j.neuron.2016.01.046. [PubMed: 26924440]
43. Hong GS, Lee B, and Oh U (2017). Evidence for Mechanosensitive Channel Activity of Tentonin 3/TMEM150C. Neuron 94, 271–273.e2. 10.1016/j.neuron.2017.03.038. [PubMed: 28426962]
44. McHugh BJ, Buttery R, Lad Y, Banks S, Haslett C, and Sethi T (2010). Integrin activation by Fam38A uses a novel mechanism of R-Ras targeting to the endoplasmic reticulum. J. Cell Sci 123, 51–61. 10.1242/jcs.056424. [PubMed: 20016066]
45. Ranade SS, Qiu Z, Woo SH, Hur SS, Murthy SE, Cahalan SM, Xu J, Mathur J, Bandell M, Coste B, et al. (2014). Piezo1, a mechanically activated ion channel, is required for vascular development in mice. Proc. Natl. Acad. Sci. USA 111, 10347–10352. 10.1073/pnas.1409233111. [PubMed: 24958852]
46. Caterina MJ, Leffler A, Malmberg AB, Martin WJ, Trafton J, Petersen-Zeitz KR, Koltzenburg M, Basbaum AI, and Julius D (2000). Impaired nociception and pain sensation in mice lacking the capsaicin receptor. Science 288, 306–313. [PubMed: 10764638]
47. Davis JB, Gray J, Gunthorpe MJ, Hatcher JP, Davey PT, Overend P, Harries MH, Latcham J, Clapham C, Atkinson K, et al. (2000). Vanilloid receptor-1 is essential for inflammatory thermal hyperalgesia. Nature 405, 183–187. 10.1038/35012076. [PubMed: 10821274]
48. Wilson SR, Gerhold KA, Bifolck-Fisher A, Liu Q, Patel KN, Dong X, and Bautista DM (2011). TRPA1 is required for histamine-independent, Mas-related G protein-coupled receptor-mediated itch. Nat. Neurosci 14, 595–602. 10.1523/jneurosci.5318-12.2013. [PubMed: 21460831]
49. Ru F, Sun H, Jurcakova D, Herbstsomer RA, Meixong J, Dong X, and Undem BJ (2017). Mechanisms of pruritogen-induced activation of itch nerves in isolated mouse skin. J. Physiol 595, 3651–3666. 10.1113/jp274199. [PubMed: 28217875]
50. Diver MM, Lin King JV, Julius D, and Cheng Y (2022). Sensory TRP Channels in Three Dimensions. Annu. Rev. Biochem 91, 629–649. 10.1146/annurev-biochem-032620-105738. [PubMed: 35287474]
51. Tominaga M (2007). The Role of TRP Channels in Thermosensation. In TRP Ion Channel Function in Sensory Transduction and Cellular Signaling Cascades, Liedtke WB and Heller S, eds. (CRC Press).
52. Hu J, and Lewin GR (2006). Mechanosensitive currents in the neurites of cultured mouse sensory neurones. J. Physiol 577, 815–828. 10.1113/jphysiol.2006.117648. [PubMed: 17038434]
53. Olsson MHM, Søndergaard CR, Rostkowski M, and Jensen JH (2011). PROPKA3: Consistent Treatment of Internal and Surface Residues in Empirical pKa Predictions. J. Chem. Theory Comput 7, 525–537. 10.1021/ct100578z. [PubMed: 26596171]
54. Ray A, Lindahl E, and Wallner B (2010). Model quality assessment for membrane proteins. Bioinformatics 26, 3067–3074. 10.1093/bioinformatics/btq581. [PubMed: 20947525]

55. Dolinsky TJ, Czodrowski P, Li H, Nielsen JE, Jensen JH, Klebe G, and Baker NA (2007). PDB2PQR: expanding and upgrading automated preparation of biomolecular structures for molecular simulations. Nucleic Acids Res 35, W522–W525. 10.1093/nar/gkm276. [PubMed: 17488841]

56. Jo S, Kim T, Iyer VG, and Im W (2008). CHARMM-GUI: A web-based graphical user interface for CHARMM. J. Comput. Chem 29, 1859–1865. 10.1002/jcc.20945. [PubMed: 18351591]

57. Jorgensen WL, Chandrasekhar J, Madura JD, Impey RW, and Klein ML (1983). Comparison of simple potential functions for simulating liquid water. J. Chem. Phys 79, 926–935. 10.1063/1.445869.

58. Eastman P, Swails J, Chodera JD, McGibbon RT, Zhao Y, Beauchamp KA, Wang L-P, Simmonett AC, Harrigan MP, Stern CD, et al. (2017). OpenMM 7: Rapid development of high performance algorithms for molecular dynamics. PLoS Comput. Biol 13, e1005659. 10.1371/journal.pcbi.1005659. [PubMed: 28746339]

59. Chow K-H, and Ferguson DM (1995). Isothermal-isobaric molecular dynamics simulations with Monte Carlo volume sampling. Comput. Phys. Commun 91, 283–289. 10.1016/0010-4655(95)00059-O.

60. Sukharev SI, Blount P, Martinac B, Blattner FR, and Kung C (1994). A large-conductance mechanosensitive channel in E. coli encoded by mscL alone. Nature 368, 265–268. 10.1038/368265a0. [PubMed: 7511799]

61. Perozo E, Cortes DM, Sompornpisut P, Kloda A, and Martinac B (2002). Open channel structure of MscL and the gating mechanism of mechanosensitive channels. Nature 418, 942–948. 10.1038/nature00992. [PubMed: 12198539]

62. Klauda JB, Venable RM, Freites JA, O'Connor JW, Tobias DJ, Mondragon-Ramirez C, Vorobyov I, MacKerell AD, and Pastor RW (2010). Update of the CHARMM All-Atom Additive Force Field for Lipids: Validation on Six Lipid Types. J. Phys. Chem. B 114, 7830–7843. 10.1021/jp101759q. [PubMed: 20496934]

63. Huang J, Rauscher S, Nawrocki G, Ran T, Feig M, de Groot BL, Grubmüller H, and MacKerell AD (2017). CHARMM36m: an improved force field for folded and intrinsically disordered proteins. Nat. Methods 14, 71–73. 10.1038/nmeth.4067. [PubMed: 27819658]

Highlights

- Mechanically gated currents of TTN3 are conserved throughout the vertebrate phyla
- Bilayer-embedded TTN3 proteins exhibit spontaneous and stretch-sensitive channel currents
- Activation threshold and pharmacological profile of TTN3 are separate from Piezo1
- A rectangular-shaped tetrameric structure and a pore at the inter-subunit center are predicted

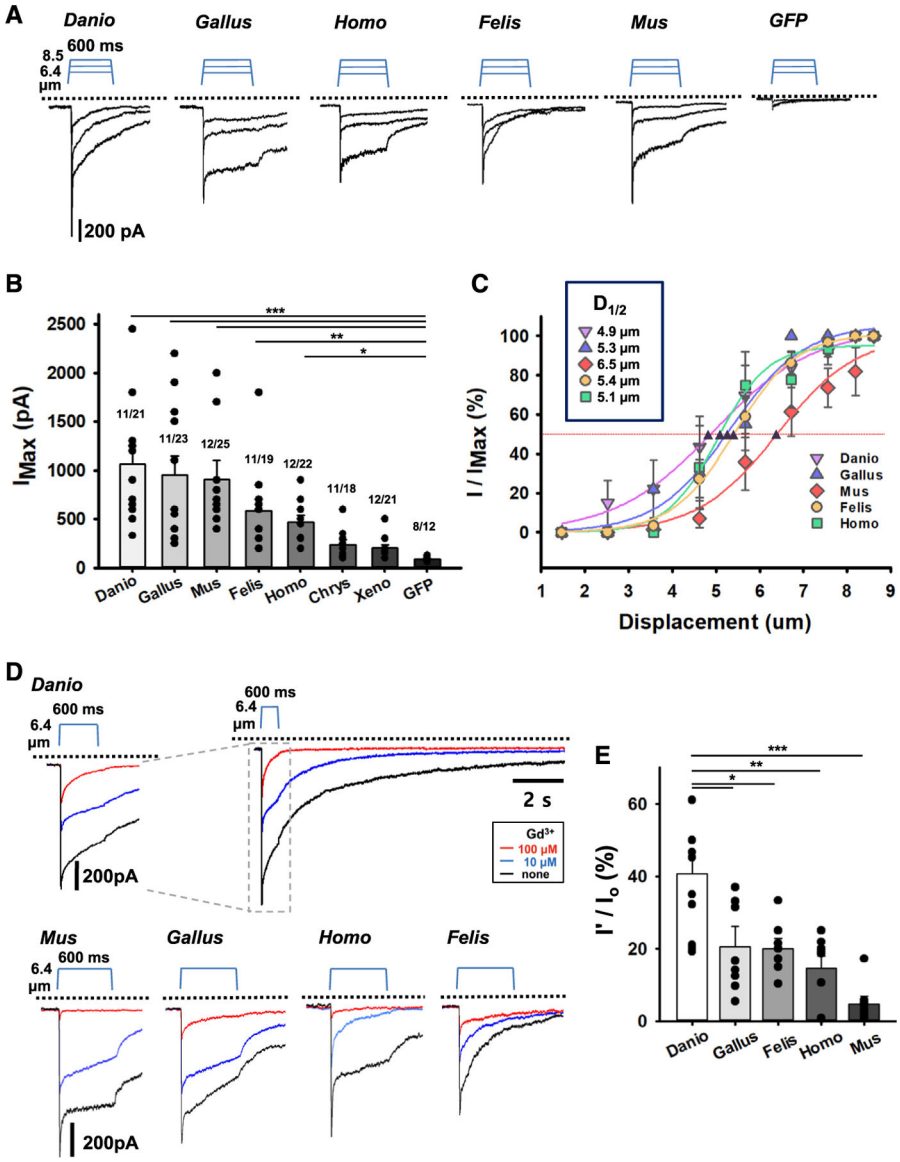

Figure 1. Mechanosensitivity of TTN3 is conserved in the vertebrate phyla

(A) Representative traces of mechanically activated (MA) currents of five TTN3 orthologs in response to mechanical step stimuli (6.4–8.5 μm). Whole-cell currents were recorded from HEK293T cells transfected with *Ttn3* orthologs and *Gfp* for control. Dotted lines represent the background currents.

(B) Summary of MA currents of the seven TTN3 orthologs in response to 8.5 μm mechanical stimulation. *Mus*, mouse; *Danio*, zebrafish; *Gallus*, chick; *Homo*, human; *Felis*, cat; *Chrys*, turtle; *Xeno*, frog. *$p < 0.05$, **$p < 0.01$, and ***$p < 0.001$; one-way analysis of variance (ANOVA) followed by Tukey's test. Data are presented as mean ± standard error of the mean (SEM).

(C) The displacement-response curves of the five TTN3 orthologs: zebrafish, chick, mouse, cat, and human. MA currents (I) were normalized by maximal peak currents (I_{Max}). Normalized currents were fitted to a Boltzmann equation. Black triangles represent

the average of the half-maximal displacement of each ortholog. Inset: half-maximal displacement ($D_{1/2}$) of the five TTN3 orthologs. Data are presented as mean ± SEM.
(D) Representative traces of MA currents of TTN3 orthologs blocked by 10 μM Gd^{3+} (blue) and 100 μM Gd^{3+} (red) with different sensitivities. Top: a representative trace of *Danio* TTN3 in expanded (left) and compressed (right) timescales.
(E) Summary of Gd^{3+} (100 μM) blocks of TTN3 orthologs. *$p < 0.05$, **$p < 0.01$, and ***$p < 0.001$; one-way ANOVA followed by Tukey's test. Data are presented as mean ± SEM.

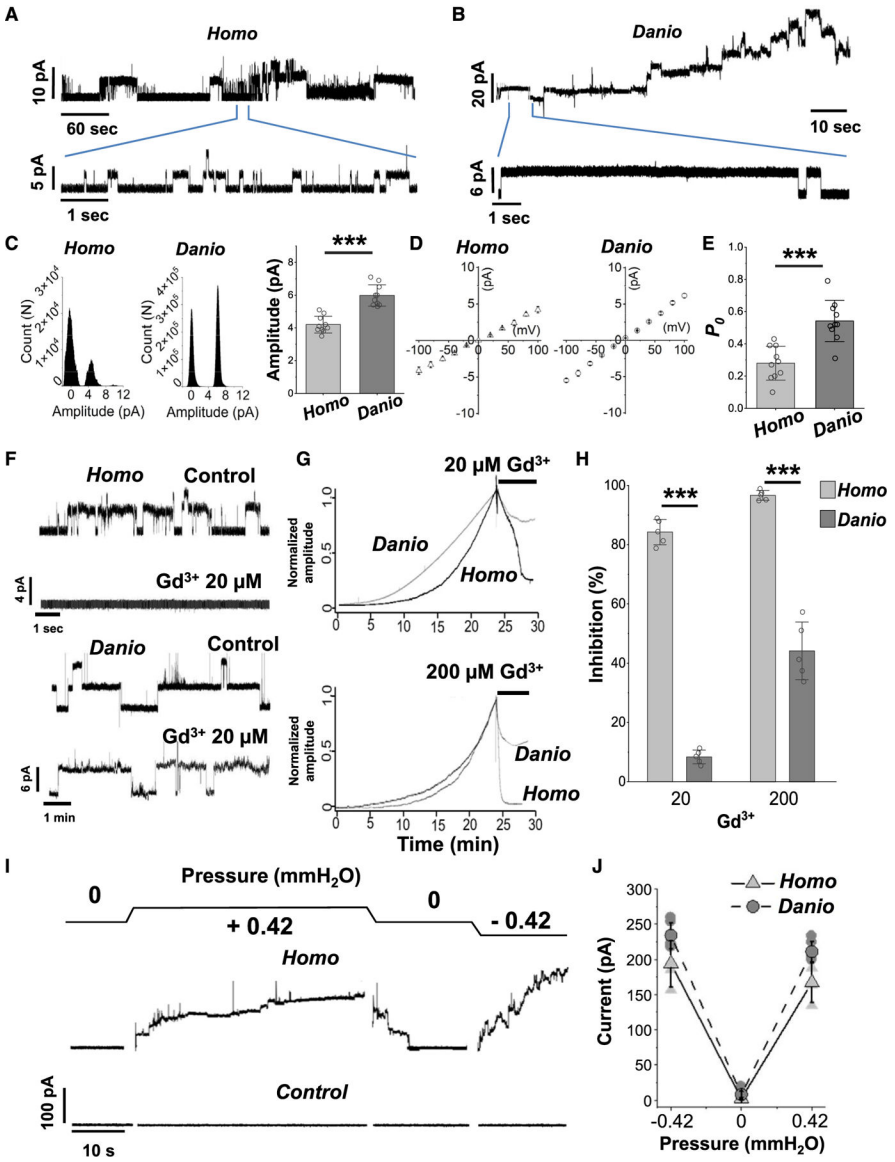

Figure 2. Spontaneous and stretch-activated single-channel currents of TTN3 proteins reconstituted in the lipid bilayer

(A and B) Representative traces of the spontaneous single-channel currents of human (*Homo*) (A) and zebrafish (*Danio*) TTN3 proteins (B) reconstituted in the 1,2-diphytanoyl-*sn*-glycero-3-phosphocholine (DPhPC) lipid bilayer. Magnification of the selected region of recording is shown on the bottom. Channel currents were recorded at +100 mV.

(C) Amplitude histograms of human and zebrafish TTN3 (left). Average amplitudes of single-channel currents of human and zebrafish TTN3 ($n = 96$ for human and 31 for zebrafish TTN3 in 10 different experiments each, right). ***$p < 0.001$, Student's t test. Data are presented as mean ± standard deviation (SD).

(D) The current-voltage relationships of the single-channel currents of human and zebrafish TTN3 ($n = 5$).

(E) Open probabilities (P_o) of spontaneous single-channel currents of human and zebrafish TTN3. ***$p < 0.001$ ($n = 10$), Student's t test. Data are presented as mean ± SD.

(F) Inhibition by 20 μM Gd^{3+} of spontaneous single-channel currents of human TTN3 (top) reconstituted in the lipid bilayer but not zebrafish TTN3 (bottom).
(G) Inhibition and partial inhibition by 20 and 200 μM Gd^{3+} of macroscopic currents in human and zebrafish TTN3 reconstituted in the lipid bilayer, respectively.
(H) Summary of the macroscopic currents of human and zebrafish TTN3 inhibited by the application of 20 and 200 μM Gd^{3+}. ***$p < 0.001$ ($n = 5$), Student's t test. Data are presented as mean ± SD.
(I) Representative traces of stretch-induced macroscopic currents of human TTN3 reconstituted in the lipid bilayer. To stretch the lipid bilayer, 20 μL of the solution (equivalent to 0.42 mmH_2O) was added to a *cis* (+) or *trans* (−) chamber. To remove the stretch, 20 μL of the solution was removed from the chamber. Control traces (bottom) represent the currents in the lipid bilayer without TTN3 protein incorporation.
(J) Summary of stretch-induced currents of human and zebrafish TTN3 ($n = 4$). Data are presented as mean ± SD.

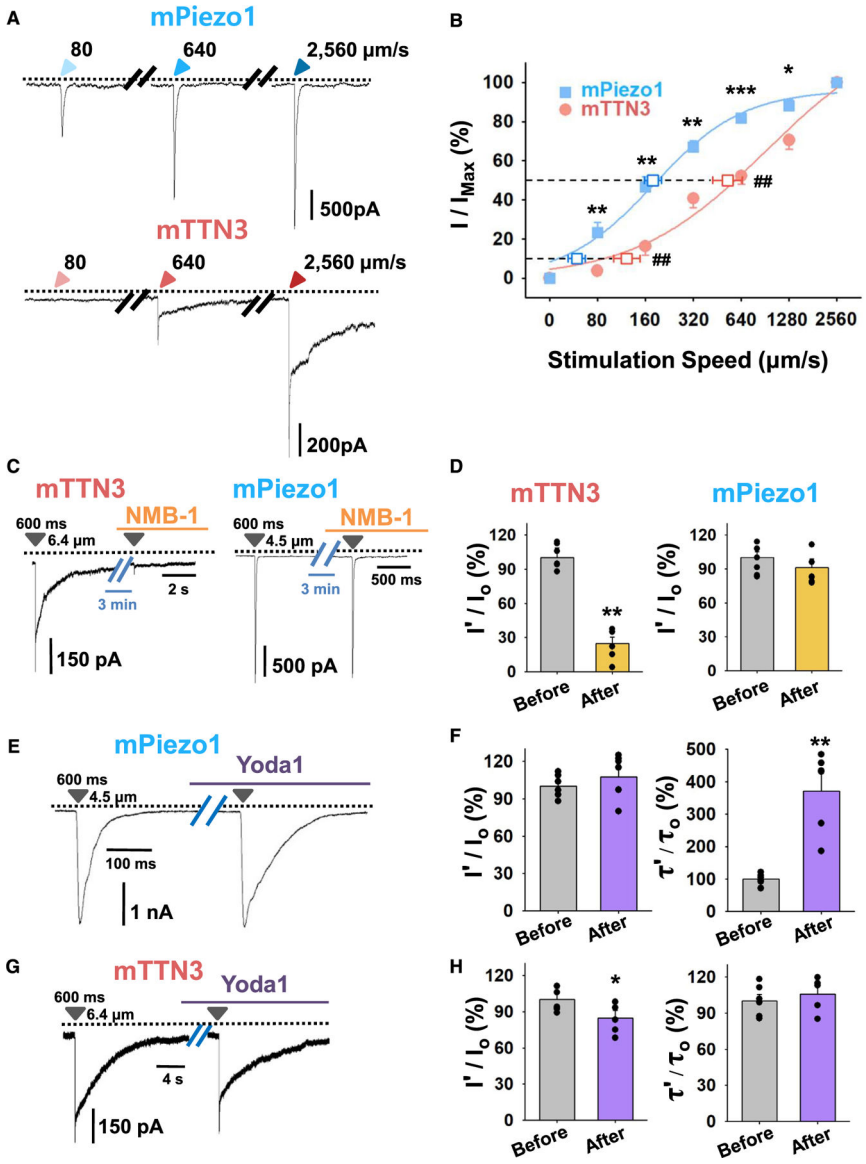

Figure 3. TTN3 mechanosensitivity is separate from Piezo1

(A) Example traces of MA currents of HEK293T cells transfected with *mTtn3* and *mPiezo1* evoked by an 8 μm step (600 ms) indentation with speeds of 80, 640, and 2,560 μm/s.

(B) Current-speed relationship of mTTN3 and mPiezo1 expressed in HEK293T cells. MA currents (I) were normalized by maximal peak currents (I_{MAX}) activated by various speeds of an 8.5 μm step stimulus. Normalized currents at each speed were fitted to a Boltzmann equation. The 10% and 50% of the maximal currents were considered the threshold and half-maximal speeds (broken lines), respectively ($n = 5$). *$p < 0.05$, **$p < 0.01$, and ***$p < 0.001$; Student's t test. Data are presented as mean ± SEM.

(C and D) Representative traces (C) and summary (D) of the effects of 10 μM NMB-1 on the mTTN3 and mPiezo1 MA currents. Mechanical steps (arrowheads, 6.4 μm, 600 ms) were applied to *mTtn3*- or *mPiezo1*-expressing HEK293T cells. I_o and I′, current amplitudes of

mTTN3 or mPiezo1 before and after NMB-1 application, respectively. $^{**}p < 0.01$; Student's t test. Data are presented as mean ± SEM.

(E) Representative traces of mPiezo1 MA currents before and after 10 μM Yoda1 application.

(F) Summary of peak MA currents (left) and inactivation-time constant (right) of mPiezo1 before (τ_o) and after (τ') Yoda1 application. $^{**}p < 0.01$; Student's t test. Data are presented as mean ± SEM.

(G) Representative traces of mTTN3 MA currents before and after 10 μM Yoda1 application.

(H) Summary of peak MA currents (left) and inactivation-time constant (right) of mTTN3 before (τ_o) and after (τ') Yoda1 application. $^{*}p < 0.05$; Student's t test. Data are presented as mean ± SEM.

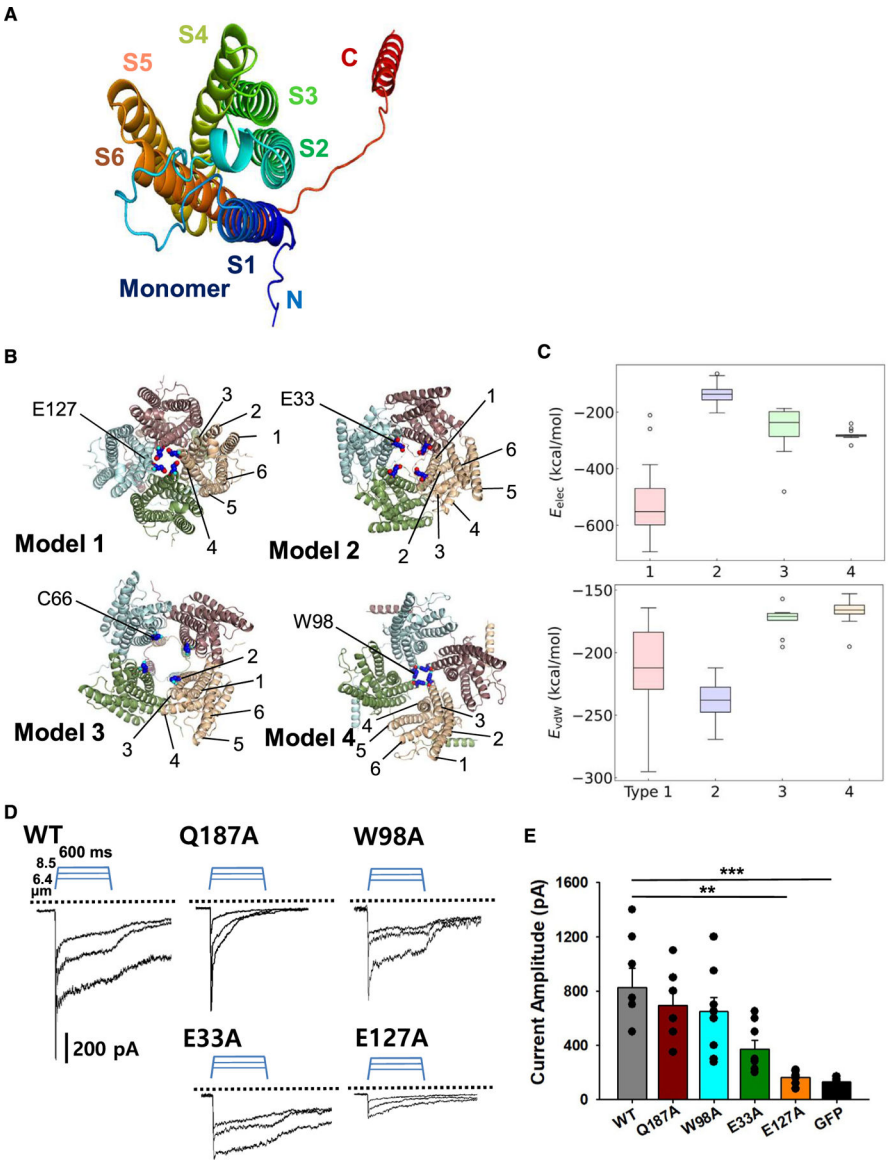

Figure 4. Monomeric and tetrameric structures of mTTN3 predicted by deep-learning-based algorithms

(A) Structure of mTTN3 monomer predicted by AlphaFold2. C, C terminus; N, N terminus; S1–S6, transmembrane helices 1–6.

(B) Four configuration models (models 1–4) of tetrameric structures of mTTN3 were predicted by the high ambiguity-driven docking program based on the molecular mechanics potential energy. Cartoon structures of the four models are shown as viewed from the top. Structures of the four representative configuration models were grouped based on their van der Waals and electrostatic energies: model 1 (n = 36), model 2 (n = 49), model 3 (n = 9), and model 4 (n = 14). Models with the lowest energy are displayed. The most constricting residues of each configuration model are shown.

(C) Boxplots of the electrostatic (top) and van der Waals (bottom) energy for the tetramer groups. The horizontal edges of the boxes denote the upper and lower quartiles, and the line in the box is the median. The lines above and below the box indicate the upper and lower

extreme values, respectively. The circles denote the outliers that are located outside 1.5 times the interquartile range above the upper quartile and below the lower quartile.

(D) Representative traces of MA currents of HEK293T cells expressing mTTN3 mutants of the residues positioned at the entry zone of putative pore of each configuration model. E_{hold} = –60 mV.

(E) Summary of current amplitudes of the mTTN3 mutants. WT (n = 9), Q187A (n = 8), W98A (n = 8), E33A (n = 8), E127A (n = 7), and GFP (n = 8). $^{**}p < 0.01$ and $^{***}p < 0.001$; one-way ANOVA followed by Tukey's test. Data are presented as mean ± SEM.

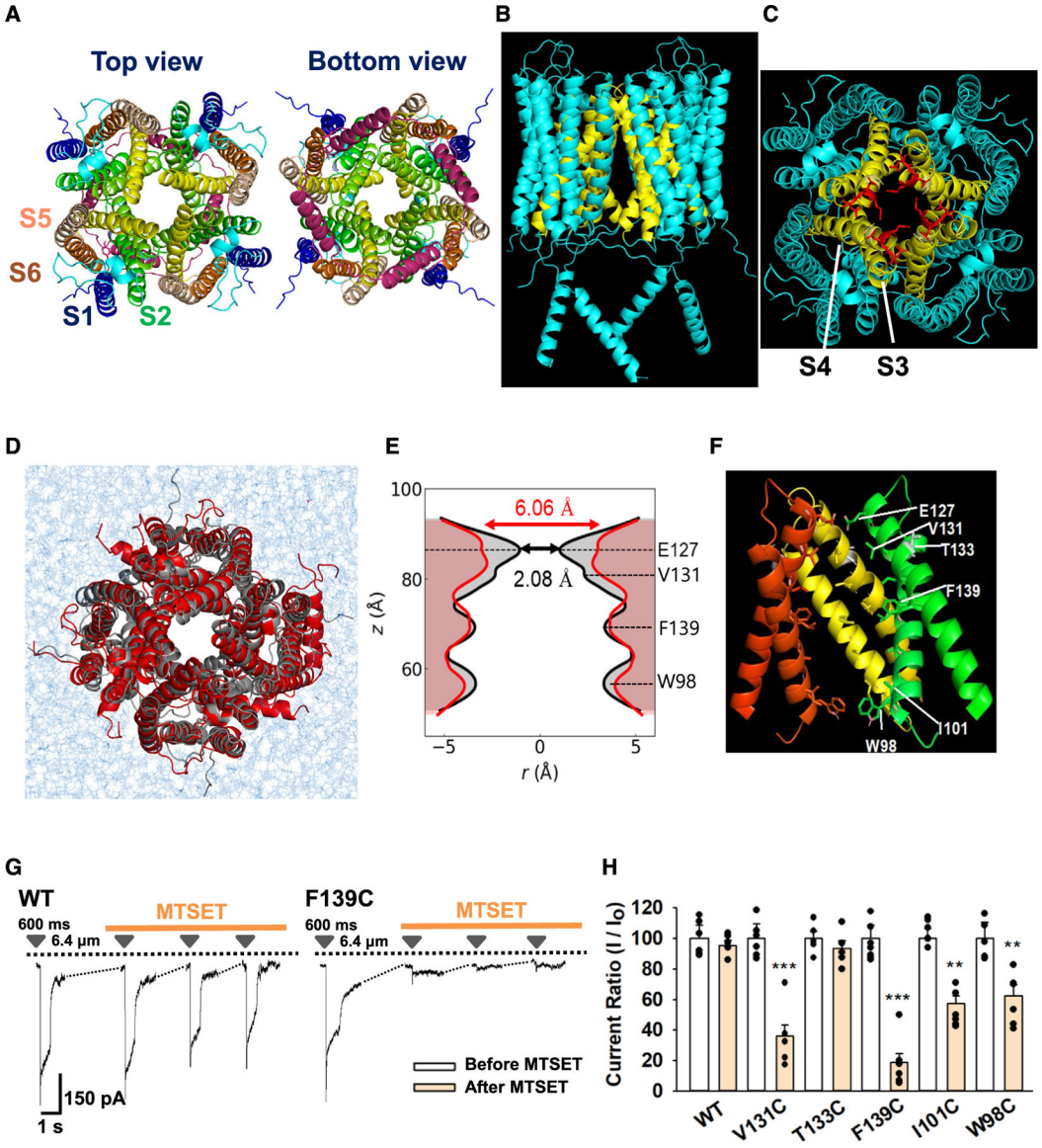

Figure 5. Predicted molecular structure and putative pore region of mTTN3

(A) Tetrameric structure of mTTN3 selected by mutagenesis among the four predicted configuration models based on molecular mechanical potential energy. Cartoon structures are shown from top and bottom views.

(B) Side view of the tetrameric mTTN3 molecule with S1, S2, S5, S6, and C-terminal helices colored in teal and S3 and S4 helices colored in yellow.

(C) Magnified top view of the putative pore region of tetrameric mTTN3. Inner helices (yellow) surrounding the central axis represent S3 and S4 domains. Negatively charged residues (DEE125–127, red) in the S4 are positioned at the entrance of the pore.

(D) Cartoon structures of mTTN3 before (gray) and after a stretch on the lipid bilayer (red, 433 ns snapshot of replica 1) from top view. Stretch was imposed into the 1,2-dioleoyl-*sn*-glycero-3-phosphocholine (DOPC) bilayer (light blue).

(E) Pore diameters in the initial (black) and active (red, 433 ns snapshot of replica 1) conformations embedded into the DOPC bilayer. Horizontal dotted lines denote four constricting sites. Each cross-sectional diameter at the constricting region was increased from 2.08 to 6.06 Å upon pulling the bilayer.

(F) The pore-lining residues constituting the mTTN3 ion permeation pathway. One monomeric subunit was removed for a better view.

(G) Representative traces of MA currents of HEK293T cells expressing wild-type (WT) and cysteine-replaced mutant F139C of mTTN3. Mechanical stimulus of 6.4 μm for 600 ms was applied before and after 1 mM MTSET application. Broken lines indicate the gap between whole-cell recordings for 1–3 min.

(H) Summary of current amplitudes of cysteine-replaced mutants of the pore-lining and T133 (F, in gray) residues. Current amplitudes of the third mechanical stimulus after MTSET application were counted for the bar graph. Data are presented as mean ± SEM. $^{**}p < 0.01$ and $^{***}p < 0.001$; Student's t test.

KEY RESOURCES TABLE

REAGENT or RESOURCE	SOURCE	IDENTIFIER
Antibodies		
Anti-TTN3 antibody	Merck	Cat# ABN2266
Anti-His tag antibody	Abcam	Cat# AB1187; RRID:AB_298652
Anti-P9 antibody	Ab frontier	Manufactured
Anti-mouse IgG secondary antibody	Sigma-Aldrich	Cat# A9044; RRID:AB_258431
Anti-rabbit IgG secondary antibody	Cell Signaling	Cat# 7074; RRID:AB_2099233
Chemicals, peptides, and recombinant proteins		
Magnesium Chloride	Sigma-Aldrich	Cat# M8266
Cesium Chloride	Sigma-Aldrich	Cat# C3139
HEPES	Sigma-Aldrich	Cat# H3375
Mg-ATP	Sigma-Aldrich	Cat# A9187
Na-GTP	Sigma-Aldrich	Cat# 51120
D-Mannitol	Sigma-Aldrich	Cat# M4125
Sodium Hydroxide	Sigma-Aldrich	Cat# S8045
Sodium Chloride	Sigma-Aldrich	Cat# S7653
Dulbecco’s Modified Eagle Medium	Gibco	Cat# 11995065
Fetal Bovine Serum	Gibco	Cat# 26140079
Penicillin/Streptomycin	Thermo Fisher Scientific	Cat# 15140122
Gadolinium	Sigma-Aldrich	Cat# 439770
NMB1	Smartox Biotechnology	Cat# NMB001-00100
Yoda1	Sigma-Aldrich	Cat# SML1558
MTSET	Biotium	Cat # 91021
Carbenicillin	Sigma-Aldrich	Cat # C1389
Chloramphenicol	Sigma-Aldrich	Cat # C0378
Bacto Yeast Extract	BD	Cat # 212750
Bactotryptone	BD	Cat # 211705
Potassium Phosphate Monobasic	Duksan	Cat # d433
Potassium Phosphate Dibasic	Duksan	Cat # d563
Glucose	Sigma-Aldrich	Cat # G8644
IPTG	Goldbio	Cat # I2481
Ammonium Sulfate	Sigma-Aldrich	Cat # A4418
EDTA	Sigma-Aldrich	Cat # E9884
Phenylmethylsulphonyl Fluoride	Sigma-Aldrich	Cat # PMSF-RO
Microfluidizer	Microfluidics	Cat # M-110P
T/G Native Sample Buffer	Koma Biotech	Cat# KTG020N
Tris base	Sigma-Aldrich	Cat# T1503
Glycine	Sigma-Aldrich	Cat# 50046
SDS	Sigma-Aldrich	Cat# L3771

REAGENT or RESOURCE	SOURCE	IDENTIFIER
Sarkosyl	Sigma-Aldrich	Cat# 61747
DOPC	Avanti	Cat# 850375
POPG	Avanti	Cat# 840457
Chloroform	Sigma-Aldrich	Cat# 366927
Amicon Ultra-0.5 Centrifugal Filter Unit	Millipore	Cat# UFC5010
Critical commercial assays		
Lipofectamine 3000	Life Technologies	Cat# L3000015
FuGene® HD	Promega	Cat# E2311
Dreamtaq Green Polymerase	Thermo Fisher Scientific	Cat# EP0712
FavorPrep Gel/PCR Purification Kit	Favorgen	Cat# FAEPK 001B
Muta-Direct Site Directed Mutagenesis Kit	LiliF Diagnostics	Cat# 15071
EZchange Site-directed Mutagenesis Kit	Enzynomics	Cat# EZ004S
NativePAGE Sample Prep Kit	Invitrogen	Cat# BN2008
Deposited data		
TTN3 monomer and tetramer models, coordinates, and Molecular Dynamics simulations	This study	Zenodo Data: https://zenodo.org/record/8176280
Experimental models: Cell lines		
Human Embryonic Kidney Cell (HEK293T)	ATCC	Cat# CRL-3216; RRID:CVCL_0063
Oligonucleotides		
PCR Primers	Table S1 in Supplemental Information	N/A
Recombinant DNA		
Mouse TTN3	Genscript	Cat# OMu08247
Zebrafish TTN3	Genscript	Cat# ODa15731
Frog TTN3	Genscript	Cat# OXa04470
Chick TTN3	Genscript	Cat# OGa35266
Turtle TTN3	Genscript	Cat# OCh161608
Cat TTN3	Genscript	Cat# OFb05814
Human TTN3	Genscript	Cat# OHu05487
Software and algorithms		
SigmaPlot 14.0	Systat	https://systatsoftware.com/sigmaplot/
PyMol Software 2.5.2	Schrodinger	https://pymol.org/2/
AlphaFold2	Jumper et al.[17]	https://github.com/deepmind/alphafold
HADDOCK Program 2.4	Van Zundert et al.[27]	https://wenmr.science.uu.nl/haddock2.4/
ProQM	Ray et al.[50]	http://www.bioinfo.ifm.liu.se/ProQM/index.php
PROPKA 3.1	Olsson et al.[51]	https://github.com/jensengroup/propka-3.1
PDB2PQR 2.1	Dolinsky et al.[52]	https://server.poissonboltzmann.org/pdb2pqr

REAGENT or RESOURCE	SOURCE	IDENTIFIER
CHARMM-GUI	Jo et al.[32]	https://charmm-gui.org/?doc=input/membrane.bilayer
OpenMM 7.6	Eastman et al.[53]	https://openmm.org